Integrin inactivation slows down neutrophils congesting the pre-metastatic lung in a model of breast cancer

Frédéric Fercoq[1,2#], Gemma S. Cairns[1#], Marco De Donatis[1,3], John B. G. Mackey[1], Alessia Floerchinger[1,4], Amanda McFarlane[1], Ximena L. Raffo-Iraolagoitia[1,3], Declan Whyte[1], Lindsey W. G. Arnott[1,3], Colin Nixon[1], Robert Wiesheu[1,3], Anna Kilbey[1,3], Leah Brown[1], Sarwah Al-Khalidi[1], Jim C. Norman[1,3], Edward W. Roberts[1,3], Karen Blyth[1,3], Seth B. Coffelt[1,3], Leo M. Carlin[1,3]*.

[1]Cancer Research UK Scotland Institute, Garscube Estate, Switchback Road, Glasgow, G61 1BD, UK

[2]Unit Communication Molecules and Adaptation of Micro-organisms (MCAM, UMR 7245), Team Parasites and Free Protistes, Muséum National d'Histoire Naturelle, CNRS; CP52, 61 rue Buffon, 75005 Paris, France

[3]School of Cancer Sciences, University of Glasgow, Garscube Estate, Switchback Road, Glasgow, G61 1QH, UK

[4]Faculty of Biosciences, University of Heidelberg, Germany.

[#]Joint first authors

*Correspondence to: Leo M. Carlin, Cancer Research UK Scotland Institute, Glasgow G61 1BD, email: leo.carlin@glasgow.ac.uk

Abstract

Neutrophils are thought to be critical to the process whereby breast cancers establish an immunosuppressive and tumour cell nurturing ‘pre-metastatic’ niche before overt metastasis can be detected. However, the spatial localization of neutrophils and their interaction with other cell types in the lung pre-metastatic niche is not well described. We used a spontaneously metastatic mammary cancer model combined with a multiplexed three- and four- dimensional imaging approach to investigate the behaviour of neutrophils in the pre-metastatic niche. Volume fixed tissue three-dimensional imaging showed that approximately 40% of $CD8^+$ T cells are adjacent to neutrophils at this stage. In live tissue, we found neutrophils with impaired intravascular motility congested the capillaries of pre-metastatic lungs potentially obstructing $CD8^+$ T cell access. Slowed neutrophil transit was dependent on conformational inactivation of β_2-integrin and could be recapitulated by treating non-tumour bearing mice with G-CSF, a potent systemic mediator of granulopoiesis. Finally, we observed differential accumulation of intravenously injected micro-beads in the lung, suggestive of transient circulatory dead spaces which were also dependent on β_2-integrin inactivation. Overall, our study proposes that integrin-mediated neutrophil congestion of the alveolar capillaries could contribute to the generation of the pulmonary pre-metastatic niche.

Introduction

Neutrophils have been linked to both pro- and anti-tumour activity based on stage and context[1] and have been mechanistically implicated in promoting breast cancer metastasis[2–4]. Tumours are known to affect their eventual site of metastasis, even before overt metastasis is detected, forming an environment termed the pre-metastatic niche[5]. Several single cell technologies have been brought to bear on the metastatic and pre-metastatic environment yielding important data on the heterogeneity and plasticity of neutrophils in cancer, but this information often lacks direct spatiotemporal information[6]. Tumours spread to the lung in approximately 30% of metastatic breast cancer patients[7,8]. The lung is a unique physiological barrier with a need for carefully balanced regulation between robust immune response and tissue damage. This balance is thought to err on the side of immunosuppression, resolution, and containment to avoid life threatening inflammation[9]. This, along with the extensive narrow vasculature acting as a filter or strainer, makes the lung a key site for metastatic seeding and outgrowth.

Therefore, we probed the behaviour of neutrophils within the lungs of mice bearing spontaneously lung metastatic mammary tumours at a stage before overt lung metastasis could be observed. Using a combination of cleared, fixed, and live *ex vivo* three- and four-dimensional multiplexed immunofluorescence imaging of lung slices we found that the pulmonary capillaries were packed with neutrophils in tumour bearing mice. $CD8^+$ T cells within this environment were almost unavoidably in close contact with the neutrophils which moved more slowly than their counterparts in the lungs of healthy mice. This change in neutrophil migratory phenotype was dependent on β_2-integrin conformational inactivation and was recapitulated by G-CSF treatment in non-tumour bearing mice. We speculate that this aberrant neutrophil intravascular motility is a by-product of phenotypically modified neutrophils from stress granulopoiesis stimulated in part by G-CSF produced by the tumour microenvironment. We suggest that these results are important to consider when targeting T cells or neutrophils in the pre-metastatic niche.

Results and discussion

‘Pre-metastatic’ lung capillaries are neutrophilic

To interrogate the lung pre-metastatic niche we used a murine model of metastatic breast cancer, where either female FVB/N mice, or Catchup$^{IVM\text{-}red}$ Ly6G neutrophil reporter mice[10], were orthotopically transplanted with mammary tumour fragments from *K14-Cre;Trp53$^{F/F}$* (KP) mice[11] (**Figure 1A**). As in the *K14-Cre;Cdh1$^{F/F}$;Trp53$^{F/F}$* (KEP) transplant model[2], tumour resection before the mice reach humane endpoint allows them to subsequently develop lung

72 metastases with complete penetrance (**Figure S1**). Therefore, prior to resection, the lungs of
73 these mice recapitulate the pre-overt metastasis microenvironment.

74 In our KP transplant model, we confirmed using flow cytometry, the presence of significant
75 neutrophilia in the pre-metastatic lung of mice with 10-15 mm orthotopic KP mammary tumours
76 (**Figure 1B, 1C and S2A**), which has been previously reported for the KEP mammary tumour
77 transplant model[2,12] and other metastatic breast cancer models such as MMTV-PyMT[3] or
78 4T1[4,13]. As we found in other metastatic models[14], neutrophilia was accompanied by an
79 increase of immature Ly6G intermediate[14] (Ly6G^{int}) neutrophils (**Figure 1D, S2B, S3A and**
80 **S3B**).

81 Neutrophils and their interaction with T cells have been implicated in breast cancer lung
82 metastasis[2], however, little is known about the location and interactions of these two cell
83 populations in the pre-metastatic lung. Thus, we used chemically cleared precision-cut lung
84 slices (PCLS) to investigate the immune landscape in the pre-metastatic lung in three
85 dimensions (3D). Spectral multiplexed immunofluorescence confocal microscopy was
86 employed to identify immune cells using six markers simultaneously in large tissue volumes
87 while preserving tissue architecture and unmixing the lungs intrinsic autofluorescence
88 (**Figures 1E and S2C**). Consistent with flow cytometry, histocytometry[15,16] of 3D multiplexed
89 images demonstrated a substantial accumulation of neutrophils in the lungs of mice with 10-
90 15 mm orthotopic KP mammary tumours, with no statistically significant increase in CD68$^+$
91 macrophage or CD8$^+$ T cell abundance (**Figures 1F, 1G**).

92 Macrophages were predominantly localized in alveoli (alveolar macrophages) or perivascular
93 adventitial spaces (interstitial macrophages) (**Figure S4A)**. Most neutrophils and CD3$^+$ T cells
94 were found within the lung vasculature, particularly in pulmonary capillaries and arteries
95 (**Figure 1H and S4A**), while neutrophils were absent from the lymphatic collectors clearly
96 apparent in podoplanin stained sections (**Figure S4B**). In contrast with controls, approximately
97 40% of CD8$^+$ T cells were directly adjacent to neutrophils in tumour bearing mice (**Figure S4C**)
98 consistent with cell-cell interactions. Notably, the proportion of T cells in contact with
99 neutrophils correlated with the number of lung neutrophils present (Spearman $r = 0.8333$
100 $p=0.0083$) (**Figure S4D**), suggesting that these interactions might be primarily mediated by
101 the significantly increased abundance of neutrophils.

102 Collectively, these findings indicate that the pre-metastatic pulmonary capillaries are
103 congested with neutrophils. This marked expansion in intravascular neutrophils may facilitate
104 interactions between neutrophils and CD8$^+$ T cells *in vivo.*

105 **Lung neutrophils do not produce oxidative burst in live PCLS from mammary tumour**
106 **bearing mice**

107 There is accumulating evidence that upon arrival in the lung, neutrophils acquire unique
108 immunosuppressive capacity to avoid damaging the delicate alveolar tree[4,17,18]. This capacity
109 is thought to be amplified in the context of tumour-driven inflammation[2,4]. Previous work
110 suggested that neutrophils could inhibit cytotoxicity of $CD8^+$ T cells in the lung through nitric
111 oxide[2]. We therefore imaged nitric oxide (NO) and superoxide (O_2^-) in live *ex vivo* PCLS to
112 investigate oxidative stress in neutrophils (as depicted in **Figures 2A and S5**). To check the
113 validity of the probes in neutrophils, we stimulated live PCLS with phorbol myristate acetate
114 (PMA) and saw expression of both NO and O_2^- in neutrophils and surrounding tissue (**Figure**
115 **S5A**). However, neither NO, nor O_2^- were detected in lung neutrophils in PCLS from control
116 or KP transplant tumour-bearing mice suggesting that this enhanced neutrophil oxidative burst
117 does not take place in the lungs at this timepoint (**Figure S5B-E**).

118 **Neutrophil motility is impaired in a CD18/ICAM-1 dependent manner in the pre-**
119 **metastatic lung**

120 Further investigation of live PCLS however revealed changes in neutrophil motility in PCLS
121 from KP transplant tumour-bearing mice compared to controls. The neutrophils from KP
122 tumour-bearing mice exhibited shorter tracks and reduced mean track speeds compared to
123 those from control mice (**Figures 2B, 2C and Video S1**) while $CD8^+$ T cells were mostly
124 immotile in both groups (**Figure S5F**). Therefore, we investigated the mechanisms which
125 control intravascular neutrophil motility in the pre-metastatic lung. Imaging studies have
126 uncovered several examples where the endpoint of leukocyte (including neutrophil):
127 endothelial interactions is not extravasation into the tissue but rather intravascular motility or
128 'patrolling'[19–21]. In addition to selectins, neutrophil β_2-integrins, Mac-1 (CD11b/CD18; $\alpha_m\beta_2$)
129 and LFA-1 (CD11a/CD18; $\alpha_L\beta_2$), with ICAM-1 (CD54) on endothelial cells are thought to
130 mediate neutrophil: endothelial cell interactions[22]. However, due to the narrow diameter of lung
131 capillaries, the typical neutrophil adhesion cascade does not occur. Instead, neutrophils are
132 forced into contact with the endothelium by constriction (**Figures 1H and S4A**). Consequently,
133 it has been postulated that integrins may not be essential for neutrophil recruitment in the
134 lung[23–25]. However, recent studies have suggested a requirement for CD11b (Mac-1) in
135 neutrophil intravascular motility[26], although it is likely that this regulation extends beyond a
136 simple relationship, as conformation and intracellular trafficking are known to regulate integrin
137 mediated binding.

138 Considering the above, we hypothesised that neutrophil intravascular motility in the lungs
139 could be attenuated by integrin inactivation. CD18 (β2), the common beta-chain for both Mac-
140 1 and LFA-1, is expressed by neutrophils at similar levels in both controls and tumour bearing
141 mice (**Figure 2D and S3C**). As integrins undergo conformational changes that govern their
142 adhesion (e.g. to ICAM-1[22] on the endothelium; **Figure 2E**), we used three monoclonal
143 antibodies to manipulate CD18-ICAM-1 interactions in the lung to investigate this putative
144 mechanism (**Figure 2E**): (1) The CD18 activating antibody (clone M18/2) stabilises the active
145 conformation of CD18, promoting adhesion to ICAM-1[27]; (2) The clone GAME-46 blocks the
146 active domain of CD18, preventing adhesion to ICAM-1[27]; and (3) The ICAM-1 blocking
147 antibody (clone YN1/1.7.4) was used to block ICAM-1. Intravenous injection of tumour cells
148 has been shown to acutely increase neutrophil numbers in lung capillaries[28]. We intravenously
149 injected a suspension of KP primary tumour cells plus GAME-46, M18/2, or isotype control
150 antibodies, and lungs were collected 30 minutes later (**Figure 2F**). Subsequently, neutrophil
151 behaviour was investigated in live PCLS and by immunohistochemistry (IHC) for Ly6G in fixed
152 lung tissue to quantify neutrophil numbers (**Figures 2G and 2H**). Notably, there was no
153 difference in neutrophil numbers in the lungs across the different treatment groups (**Figures**
154 **2G and 2I**). However, CD18 blocking with GAME-46 reduced neutrophil speed, whereas
155 M18/2 increased neutrophil speed compared to isotype control (**Figures 2H and 2J, Video**
156 **S2**). Likewise, intravenous injection of KP tumour cells with ICAM-1 blocking antibodies or
157 isotype control did not impact neutrophil numbers but blocking ICAM-1 inhibited neutrophil
158 movement in live PCLS (**Figure S6**).

159 These results suggest that β2-integrins could be critical modulators of tumour mediated
160 neutrophil motility in the pre-metastatic lung. Therefore, to investigate whether CD18
161 conformational stabilisation altered neutrophil speed in the lungs of mice with distant
162 orthotopic KP tumours, we treated live PCLS from control and KP transplant tumour-bearing
163 mice with M18/2 *ex vivo* (**Figure 2K**). Antibody treatment had no significant impact on
164 neutrophil motility in control PCLS; however, M18/2 was able to restore neutrophil crawling
165 speed in PCLS from tumour-bearing mice (**Figures 2L, 2M and S7A**). This suggests that
166 tumour-driven neutrophil motility impairment can be mediated by conformational inactivation
167 of CD18.

168 **G-CSF recapitulates decreased lung neutrophil motility**

169 We next investigated the potential mediator of CD18 conformational change. It is well-known
170 that breast cancers induce neutrophilia through G-CSF[2–4]. We therefore hypothesized that G-
171 CSF may be responsible for CD18 inactivation in addition to neutrophil accumulation. Mice
172 were administered a single 5 μg dose of G-CSF intraperitoneally, and the lungs were collected

173 24 hours later to analyse neutrophil motility in *ex vivo* live PCLS and neutrophil abundance by
174 IHC or flow cytometry (**Figure 3A**). Lung neutrophil numbers were increased following G-CSF
175 treatment (**Figures 3B and 3C**), with a significant increase in the number of immature Ly6G
176 intermediate[14] (Ly6G^{int}) neutrophils (**Figure 3D**). In live PCLS, neutrophil behaviour
177 recapitulated that observed in tumour-bearing mice **(Figures 3E and 3F vs. 2M**). Notably,
178 neutrophil speed was reduced in G-CSF-treated mice, which could be rescued with M18/2
179 (**Figures 3E, 3F and S7B**). Therefore, it is possible that G-CSF contributes to the alteration
180 of neutrophil motility in tumour-bearing mice consistent with the reduction in pro-metastatic
181 neutrophils that has been previously observed upon blocking G-CSF in mammary tumour
182 bearing mice[2].

183 **Slow moving neutrophils alter blood flow**

184 Finally, we aimed to determine the consequences of neutrophilia and neutrophil speed
185 impairment in lung vasculature. In the context of the work above, we hypothesized that
186 neutrophils could (1) favour the arrest of circulating tumour cells arriving in lung capillaries as
187 neutrophils have been shown to interact with tumour cells in liver sinusoids and favour their
188 arrest[29,30]; and (2) neutrophils could affect normal blood circulation, as it has been shown that
189 neutrophils can obstruct capillaries in the brain[31,32] and lung[33], impairing blood flow and
190 creating transient circulatory dead spaces.

191 Therefore, we intravenously administered fluorescent beads with a diameter of 10 µm (larger
192 than typical lung capillary size) and 4 µm (slightly smaller than a red blood cell) to control and
193 KP tumour-bearing mice to both 'model' tumour cells and to have a readout of lung blood
194 volume respectively (**Figure 4A**). In addition, mice were treated with either M18/2 or isotype
195 control antibodies to determine whether restoring neutrophil motility affects bead retention in
196 the lung (**Figure 4A**). IHC staining for Ly6G on lung tissue did not indicate a significant
197 difference in neutrophil accumulation in the lungs of tumour-bearing mice treated with isotype
198 control or M18/2 antibody (**Figures 4B and 4C**), in line with what we had observed in the IV-
199 injection model (**Figures 2F and 2I**). 3D fluorescence imaging of fixed PCLS revealed that the
200 retention of 10 µm beads remained unaffected by the presence of primary tumours or antibody
201 treatment, likely due to physical entrapment in the capillaries (**Figures 4D and 4E**). However,
202 significantly fewer 4 µm beads were found in PCLS from tumour-bearing mice treated with
203 isotype control when compared with control mice, supporting the idea of transient formation of
204 circulatory dead spaces in the lung reducing total blood volume (**Figure 4F**). Interestingly,
205 treatment with M18/2 antibody was able to restore a similar bead count to that from control
206 mice, suggesting that restoring neutrophil motility also restores blood circulation (**Figure 4F**).

207 The formation of transient poorly perfused spaces could prevent efficient immune surveillance
208 and enhance tumour cell seeding, supporting a true 'pre-metastatic niche'.

209 Taken together, our results suggest that when primary mammary tumours induce substantial
210 systemic neutrophilia, this aberrant and potentially less mature neutrophil population fail to
211 activate the β_2-integrins that would allow normal intravascular motility, causing congestion and
212 impairment of local blood circulation. That this can be recapitulated by treatment of G-CSF to
213 non-tumour bearing mice suggests a role for this potent mediator of neutrophil homeostasis,
214 known to be increased in the tumour microenvironment of mammary tumours[12].

215 In the context of breast cancer metastasis, impaired intravascular neutrophil motility,
216 congestion and reduced local circulatory flux could offer niches inaccessible to anti-tumour
217 immune cells and promote tumour cell seeding. Additionally, CD11b/CD18 has also been
218 implicated in neutrophil antibody-dependent cellular cytotoxicity (ADCC) of tumour cells[34].
219 Inactivation of neutrophil integrins could therefore provide another mechanism of immune
220 escape mediated by the primary tumour to favour metastasis at distant sites.

221 Materials & Methods

222 Mice

223 Either female FVB/N mice purchased from Charles River Laboratories (acclimatised for at
224 least 1 week in our mouse facility), or female Catchup$^{IVM\text{-}red}$ mice[10] (identified as *Ly6G*$^{Cre\text{-}tom/+}$
225 *ROSA26*$^{tdtom/+}$, backcrossed onto a FVB/N background for >10 generations and bred in-house)
226 were used for experiments when they were 8-15 weeks old. Age matched mice were randomly
227 allocated to control and transplant/treatment groups. How specific cohorts were analysed is
228 described in the appropriate methods sections and figure legends.

229 Mice were housed (as in [14]) at the CRUK Scotland Institute, UK in specific pathogen-free
230 conditions with a 12 hr light/dark cycle and at a controlled climate of 19-22 °C and 45-65 %
231 humidity. Mice also had access to food and water ad libitum. Mouse procedures were
232 performed in accordance with the UK Animal (Scientific Procedures) Act 1986, approved by
233 the local animal welfare (AWERB) committee, and conducted under UK Home Office licences
234 (PP6345023, P72BA642F and PP0826467) at the CRUK Scotland Institute.

235 Tumour models

236 *Pre-metastatic lung induction.* To induce a pre-metastatic lung, 1 mm^3 mammary tumour
237 fragments obtained from *K14-Cre;Trp53*$^{F/F}$ (KP) mice (maintained on an FVB/N background)[11]

238 were orthotopically transplanted into the 4th mammary fat pad of 10-12 week old female
239 recipient FVB/N or CatchupIVM-red mice using anaesthesia and analgesia. The tumour
240 pieces were allowed to develop into a primary mammary tumour of 10-15 mm in any direction
241 measured three times a week using a calliper and mice were humanely killed usually within a
242 month after transplant. Control mice did not undergo transplantation but were kept in the same
243 conditions.

244 *IV injection models.* For intravenous injection, sub-confluent KP cells, initially obtained from a
245 mammary KP tumour as described before[35], were washed, trypsinized, centrifuged (300 g, 5
246 min), resuspended in medium (RPMI) and passed through a 70 µm cell strainer (Greiner Bio-
247 One). The cells were counted using the CellDrop cell counter (DeNovix), diluted to a maximal
248 concentration of 10^6 cells per mL if necessary and stained with CellTrace (Invitrogen)
249 according to the manufacturer's protocol (Invitrogen). Briefly, cells were incubated with 1 µM
250 CellTrace yellow or far-red in PBS for 20 min at 37 °C. The suspension was then diluted
251 fivefold with culture medium (RPMI) and incubated for 5 min to remove free dye in the solution.
252 Finally, the suspension was centrifuged (300 g, 5 min) and resuspended in PBS before mice
253 were injected intravenously with 100 µL of suspension of $0.5x10^6$ cells and 10 µg of
254 monoclonal antibodies. The following low endotoxin, azide-free purified antibodies were used:
255 isotype control (clone RTK2758, Biolegend), ICAM-1 blocking antibody (clone YN1/1.7.4,
256 Biolegend), CD18-activating antibody (clone M18/2, Biolegend), CD18-blocking antibody
257 (clone GAME-46, BD biosciences).

258 **G-CSF treatment**

259 Female CatchupIVM-red and FVB/N mice aged 8-15 weeks were treated with 5 µg mouse
260 recombinant G-CSF (STEMCELL Technologies) by intraperitoneal injection (i.p.) 24 hours
261 before harvesting the stated tissues.

262 **Flow cytometry**

263 Lungs were excised and then minced with scissors before incubation in RPMI (ThermoFisher)
264 with 10% foetal bovine serum (FBS, ThermoFisher) at 37 °C for 20 min with agitation. Post-
265 incubation, lungs were mashed through a 70 µm filter.

266 Single cell suspensions were stained with Live/Dead stain (LIVE/DEAD Fixable Near-IR,
267 Yellow or Green, Biolegend) and Fc-Receptor block was performed (clone 93, Biolegend).
268 Cell suspensions were incubated with directly conjugated fluorescent antibodies in PBS/1%
269 (w/v) BSA (Merck)/0.05% (v/v) Sodium Azide (GBiosciences) (PBA) buffer at 4 °C for 30 min.

270 Count beads (CountBright, Life Technologies) were used to determine cell numbers.
271 Compensation was performed using single stained beads (Ultracomp eBeads, ThermoFisher).
272 Acquisition was performed on a BDFortessa using FacsDiva software (BD Biosciences) and
273 data were analysed using FlowJo software (BD).

274 The following antibodies were used:

275 Lung immunophenotyping panel: (all 1/200): CD8-AF488 (clone 53-6.7, Biolegend), CD45-
276 BV711 (clone 30-F11, Biolegend), CD11b-BV650 (clone M1/70 Biolegend), SiglecF-BV605
277 (clone E50-2440 BD Biosciences), F4/80-BV510 (clone BM8, Biolegend), B220-BV421, Ly6G-
278 BUV395 (clone 1A8, BD Biosciences), CD3-AF657 (clone 17A2, Biolegend), CD4-PE/Cy7
279 (clone RM4-5, Biolegend).

280 Neutrophil phenotyping panel 1: Ter119-FITC (clone TER-119 Biolegend 1:200), NKp46-FITC
281 (clone 29A1.4 Biolegend 1:200), CD115-AF488 (clone AFS98 Biolegend 1:200), CD3-FITC
282 (clone 17A2 Biolegend 1:200), CD19-FITC (clone 6D5 Biolegend 1:200), CD45-BV650 (clone
283 30-F11 Biolegend 1:200), CD11b-BV605 (clone M1/70 Biolegend 1:400), Ly6G-BV510 (clone
284 1A8 Biolegend 1:200), Siglec-F-APC-Cy7 (clone E50-2440 BD Biosciences 1:200), CD18-
285 AF647 (clone M18/2 Biolegend 1:200).

286 Neutrophil phenotyping panel 2: Ter119-FITC (clone TER-119 Biolegend 1:200), NKp46-FITC
287 (clone 29A1.4 Biolegend 1:200), CD115-AF488 (clone AFS98 Biolegend 1:200), CD3-FITC
288 (clone 17A2 Biolegend 1:200), CD19-FITC (clone 6D5 Biolegend 1:200), SiglecF-AF488
289 (clone 1RNM44N Invitrogen 1:200), CD45-BV650 (clone 30-F11 Biolegend 1:200), CD11b-
290 BV605 (clone M1/70 Biolegend 1:400), Ly6G-BV510 (clone 1A8 Biolegend 1:200), CD18-
291 AF647 (clone M18/2 Biolegend 1:200).

292 **Fixed PCLS imaging**

293 Precision-cut lung slices (PCLS) were prepared as previously described [36–38]. Mice were
294 humanely killed by overdose of anaesthetic (i.p. injection of sodium-pentobarbital) followed by
295 permanent cessation of the circulation by cutting the femoral artery. A blunted 22G needle
296 was then inserted via a tracheostomy and used to inflate the lungs slowly but continuously
297 with 1 mL of 2% low-melting point agarose (ThermoFisher) prepared in PBS. When flow
298 cytometry of lung tissue was to be performed on the same animals, the left lung was tied off
299 with a suture before lung inflation. Using suture thread, the trachea was then tied to stop
300 agarose leakage before excising lungs, heart and trachea together and placing them in ice-
301 cold PBS. They were then subsequently fixed in 4% formaldehyde (v/v) (FA) in PBS
302 (ThermoFisher) for two hours or overnight. 300 µm lung tissue sections were sliced using a

303 vibrating microtome (5100mz; Campden Instruments) and stainless-steel blades (Model 7550-
304 1-SS; Campden Instruments) with the highest oscillation amplitude, maximal speed, and an
305 advance of 1 mm/sec. Lung sections were stored in PBA at 4°C. For permeabilization and
306 blocking, samples were incubated in 300 µL permeabilization buffer (PBS, 1% BSA, 0.05%
307 Azide, 10% NGS, 0.3% Triton X 100) for at least one hour. Slices were rinsed with wash buffer
308 (PBS, 1% BSA, 0.05% Azide, 0.1% Triton X 100) before staining with primary antibodies
309 diluted in antibody buffer (PBS, 1% BSA, 0.05% Azide, 10% NGS, 0.1% Triton X 100).
310 Incubation at room temperature in the dark was allowed for at least 3 hours or overnight before
311 washing three times with wash buffer at 37 °C for at least 20 min each. Directly conjugated
312 antibodies, secondary antibodies, and nuclear stains (DAPI or Draq5, 1:1000) diluted in
313 antibody buffer were incubated with the samples for at least 3 h in the dark. If primary and
314 directly conjugated antibodies were derived from the same species (i.e. rat), they were not
315 stained simultaneously. In this case, the slices were washed as above after incubation with
316 the secondary antibody and free antigen binding sites were blocked with appropriate isotype
317 to avoid binding of the secondary antibody to the subsequently used directly conjugated
318 antibodies. Slices were washed twice as above and once with PBS before fixation with 4% FA
319 for 5 mins. FA was removed with two PBS washes before tissue clearing was performed.
320 Clearing with Ce3D including the preparation of the clearing solution has previously been
321 described in detail[16,39]. Briefly, N-methylacetamide was melted and diluted in PBS to prepare
322 a 40% (v/v) stock solution. 86% Histodenz (w/v) was added and allowed to fully dissolve by
323 incubation at 37 °C in a shaking incubator. 0.1% (v/v) Triton X 100 and 0.5% (v/v) 1 thioglycerol
324 were added. Slices were immersed in Ce3D and incubated at room temperature until sufficient
325 clearing was observed. The tissue sections were mounted on microscope slides (VWR) in
326 Ce3D using Frame Seal incubation chambers (Bio Rad) and kept at 4°C in the dark after
327 coverslipping (thickness no. 1.5; VWR). Slices were imaged on a Zeiss LSM 880 confocal
328 microscope using a 32 channel Gallium arsenide phosphide (GaAsP) spectral detector with
329 plan Apo objective lenses (20X/0,8 NA - dry, Carl Zeiss). Samples were excited
330 simultaneously with 405, 488, 561 and 633 laser lines and signal was collected onto the
331 arrayed GaAsp detector in lambda mode with a resolution of 8.9 nm over the visible spectrum.
332 Using reference spectra acquired from either unstained tissue for autofluorescence or single
333 stained tissue for each antibody listed below, the images were then spectrally unmixed using
334 Zen software (Carl Zeiss).

335 The following primary antibodies were used: Hamster anti-mouse CD31 (1/400, clone 2H8,
336 Invitrogen), rat anti-mouse CD8 (1/200, 14-0808-82, ebioscience), S100A9 (1/1000,
337 EPR22332-75, Abcam).

338 The following secondary antibodies were used: Goat Anti-Armenian Hamster polyclonal IgG
339 conjugated with AF488 (1/400, Jackson Immunoresearch), Goat Anti-Rat IgG conjugated with
340 Cy3 (1/400, Jackson Immunoresearch), Goat anti-Rabbit IgG conjugated with AF700 (1/400,
341 Invitrogen). Antibodies with minimal Cross Reactivity to human, bovine, horse, mouse and
342 rabbit serum proteins were preferred.

343 The following conjugated antibodies were used:

344 Anti-mouse I-A/I-E conjugated with BV421 (1/200, clone M5/114.15.2, Biolegend), anti-mouse
345 Podoplanin conjugated with AF488 (1/200, clone PMab-1, Biolegend), anti-mouse CD3
346 conjugated with AF488 (1/200, clone 17A2, Biolegend), anti-mouse CD68 conjugated with
347 AF594 (1/400, clone FA-11, Biolegend)

348 **Cell segmentation and histocytometry analysis**

349 For histocytometry analysis, the method previously published by Li et al.[16] was adapted to the
350 specific needs of the experiment. Gaussian filtering in Imaris was applied on the channels of
351 interest representing specific cell types. Summing was used to generate a merged channel
352 with all stained cell types using the Channel Arithmetic function in Imaris. Multiplier factors
353 served to normalize the channels to one another and obtain similar intensities for all markers
354 in the composite channel. Surface objects were created with the respective module in Imaris.
355 The surface detail in the smooth function was set to 1.4 µm. Background correction was
356 enabled to allow segmentation based on local contrast in areas with differing background
357 intensities such as bronchi with high autofluorescence. A threshold was set to incorporate all
358 cell derived signals while excluding unspecific background. The split touching objects option
359 was enabled and set to 8 µm, i.e. the approximate mean size of the observed cell types. Seed
360 points were filtered to only include events with sufficient signal intensity. After verifying an
361 adequate representation of the cells of interest by the created surface objects, the statistics
362 for these objects were exported into CSV files.

363 Relevant parameters were combined into one Excel file applying the RDBMerge plugin
364 (http://www.rondebruin.nl/win/addins/rdbmerge.htm) for automation of the process. In our
365 experiments, mean and summed channel intensity, volume, area, and position are the crucial
366 parameters. These data were saved in a CSV file which can subsequently be opened in
367 FlowJo for phenotypic gating and quantification of different cell populations like typical flow
368 cytometry analysis.

369 Interactions between stained $CD8^+$ T cells and $Ly6G^+$ Neutrophils were quantified based on
370 the distance between one cell and the nearest cell of the other cell type. To achieve this, spots

371 and surface objects were generated in Imaris for both cell types respectively and the 'Find
372 spots close to surface' XTension was used to define the subset of cells that interact with the
373 other cell type, i.e. spots that are within the set threshold distance of 8 µm from a surface
374 object.

375 **Live PCLS imaging**

376 All mice used for neutrophil dynamics analysis were humanely killed within the same period
377 (between 09.00-10.30) to minimize circadian-induced changes between samples. Where
378 cohorts needed to be split over several imaging sessions, each imaging session was carried
379 out with at least one age-matched control. Live PCLS procedure was performed as in [36]. Lungs
380 were inflated with low melting agarose point as above. Excised lungs were placed in ice-cold
381 PBS. Lungs were sliced into 300µm thick sections on a vibratome and stained with directly
382 conjugated antibodies, Hoechst and probes for reactive superoxide and nitric oxide (ROS-ID®
383 ROS/RNS detection kit, Enzo Life Sciences) in complete medium (phenol-red free DMEM
384 substituted with 10% FBS) for 20 minutes at 37°C. For *ex vivo* integrins activation experiments,
385 isotype control (clone RTK2758, Biolegend) or CD18-activating (clone M18/2, Biolegend)
386 antibodies were added to the solution at 1/50 dilution.

387 The following antibodies were used (all 1/200): Anti-mouse CD31-BV421 (clone 390,
388 Biolegend), anti-mouse CD8-AF488 (clone 53-6.7, Biolegend), anti-mouse Ly6G-DyLight550
389 (clone 1A8, Novus Biologicals), anti-mouse CD11c-AF594 (clone N418, Biolegend), anti-
390 mouse CD45 Spark NIR685 (clone 30-F11, Biolegend).
391
392 Slices were imaged on a Zeiss LSM880 confocal microscope using multiwell incubation
393 chambers (Ibidi µ-Slide 8-well or Nunc Lab-Tek II 8-well Chamber Slide System) at 37°C with
394 5% CO2. Lung slices were imaged for 6 to 40min with z-stacks of 22-35µm. Acquisition was
395 performed with a 32 channel Gallium arsenide phosphide (GaAsP) spectral detector plan Apo
396 objective lenses (20X/0,8 NA - dry, Carl Zeiss). Samples were excited simultaneously with
397 405, 488, 561 and 633 laser lines and signal was collected onto a linear array of the 32 GaAsp
398 detectors in lambda mode with a resolution of 8.9 nm over the visible spectrum. Spectral
399 images were then unmixed with Zen software (Carl Zeiss) using reference spectra acquired
400 from unstained tissues (tissue autofluorescence) or slides containing single fluorophores.

401 **4D image analysis**

402 Timelapse image analysis and visualization was performed using Imaris (Bitplane).
403 Neutrophils and $CD8^+$ T cells were segmented and tracked using the 'surface' tool using either

404 Ly6G fluorescence intensity (neutrophils) or CD8 (T-cells). All surfaces and tracks were
405 checked manually to avoid any false detections. Oxidative stress was measured with
406 superoxide/nitric oxide mean cell fluorescence and cell behaviour was determined using the
407 mean track speed.

408 **Immunohistochemistry (IHC)**

409 Lungs were fixed in 4% buffered formalin overnight. Fixative was changed 24 h post-fixation
410 for a further 24 h. Thereafter, lungs were dehydrated in increasing concentrations of 70% to
411 100% ethanol, and then placed in xylene before paraffin embedding. Four-micron-thick serial
412 sections were prepared as previously published[38]. Immunostaining for neutrophils was
413 performed at the CRUK Scotland Institute's Histology Facility. Antigen retrieval was performed
414 using ER2 retrieval buffer (20 min, 95 °C). Sections were then stained for Ly6G (clone 1A8)
415 at a previously optimized dilution (1/60000) for 30 min at room temperature with the
416 autostainer Bond Rx (Leica Microsystems GmbH, Wetzlar, Germany). The IHC sections were
417 visualised with 3,3'Diaminobenzidine (DAB). Stained sections were then digitally scanned
418 using a Leica Aperio AT2 slide scanner at ×20 magnification. Digital slides were analysed with
419 QuPath[40]. Lung sections were annotated using 'pixel classification' and DAB positive cells
420 within the annotated areas were detected using the "positive cell detection" tool. Results were
421 then expressed as the number of positive cells/mm^2 of lung tissue.

422 **Fluorescent beads retention in the lung**

423 Once outgrown tumours reached 12mm in any direction, mice were injected intraperitoneally
424 with 20µg of CD18 activating antibody (clone M18.2, Biolegend) or Isotype control (clone
425 RTK2758, Biolegend) in 100µL PBS. 24h later, mice were injected intravenously with a 100µL
426 mixture containing 10µg of CD18 activating antibody or isotype control, 500 000 blue-
427 fluorescent Polystyrene Microspheres, diameter 10 µm (FluoSpheres, Thermofisher) and
428 20uL of a solution (2% solids) of yellow/green-fluorescent Sulfate Microspheres, diameter 4.0
429 µm (FluoSpheres, Thermofisher). Mice were culled for lung collection 15 minutes after
430 injection and lung were processed for fixed PCLS imaging (see above). Cleared PCLS were
431 imaged using an Opera Phenix (Perkin Elmer) high throughput spinning disk microscope.
432 Images were analysed using Imaris (Bitplane) to measure the number of beads / mm^3 in the
433 lung sections.

434 **Statistics**

435 Representation and data analysis were performed with Prism 9.0 and 10.0 software
436 (GraphPad Inc.). The choice of statistical analysis was based on sample size and distribution

437 of samples. Normality was assessed via the Shapiro–Wilk test. Data from independent
438 experiments were pooled when possible. For normally distributed data (1) parametric t-tests
439 were used to compare two groups; (2) One-way analysis of variance (ANOVA) was used to
440 compare three groups according to one variable (antibody treatment) and (3) Two-way
441 ANOVA, followed with Sídák's multiple comparisons tests was performed to analyse the
442 influence of two independent variables (tumour presence and/or antibody treatment). Results
443 from normally distributed data are expressed as mean +/- standard error to the mean (SEM).
444 Specific numbers of animals can be found in corresponding figure legends.

445 ## References

446 1. McFarlane, A. J., Fercoq, F., Coffelt, S. B. & Carlin, L. M. Neutrophil dynamics in the
447 tumor microenvironment. *J. Clin. Invest.* **131**, (2021).
448 2. Coffelt, S. B. *et al.* IL-17-producing γδ T cells and neutrophils conspire to promote breast
449 cancer metastasis. *Nature* **522**, 345–348 (2015).
450 3. Wculek, S. K. & Malanchi, I. Neutrophils support lung colonization of metastasis-initiating
451 breast cancer cells. *Nature* **528**, 413–417 (2015).
452 4. Gong, Z. *et al.* Immunosuppressive reprogramming of neutrophils by lung mesenchymal
453 cells promotes breast cancer metastasis. *Sci. Immunol.* **8**, (2023).
454 5. Maru, Y. The lung metastatic niche. *J. Mol. Med.* **93**, 1185–1192 (2015).
455 6. Quail, D. F. *et al.* Neutrophil phenotypes and functions in cancer: A consensus statement.
456 *J. Exp. Med.* **219**, (2022).
457 7. Xiao, W. *et al.* Risk factors and survival outcomes in patients with breast cancer and lung
458 metastasis: a population-based study. *Cancer Med.* **7**, 922–930 (2018).
459 8. Chen, M.-T. *et al.* Comparison of patterns and prognosis among distant metastatic breast
460 cancer patients by age groups: a SEER population-based analysis. *Sci. Rep.* **7**, 9254
461 (2017).
462 9. Snelgrove, R. J., Godlee, A. & Hussell, T. Airway immune homeostasis and implications
463 for influenza-induced inflammation. *Trends Immunol.* **32**, 328–334 (2011).
464 10. Hasenberg, A. *et al.* Catchup: a mouse model for imaging-based tracking and
465 modulation of neutrophil granulocytes. *Nat. Methods* **12**, 445–452 (2015).
466 11. Liu, X. *et al.* Somatic loss of BRCA1 and p53 in mice induces mammary tumors with
467 features of human BRCA1-mutated basal-like breast cancer. *Proc. Natl. Acad. Sci.* **104**,
468 12111–12116 (2007).
469 12. Wellenstein, M. D. *et al.* Loss of p53 triggers WNT-dependent systemic inflammation
470 to drive breast cancer metastasis. *Nature* **572**, 538–542 (2019).

471 13. Li, P. *et al.* Lung mesenchymal cells elicit lipid storage in neutrophils that fuel breast
472 cancer lung metastasis. *Nat. Immunol.* **21**, 1444–1455 (2020).
473 14. John B. G. Mackey *et al.* Maturation, developmental site, and pathology dictate
474 murine neutrophil function. *bioRxiv* (2021).
475 15. Gerner, M. Y., Kastenmuller, W., Ifrim, I., Kabat, J. & Germain, R. N. Histo-
476 Cytometry: A Method for Highly Multiplex Quantitative Tissue Imaging Analysis Applied to
477 Dendritic Cell Subset Microanatomy in Lymph Nodes. *Immunity* **37**, 364–376 (2012).
478 16. Li, W., Germain, R. N. & Gerner, M. Y. High-dimensional cell-level analysis of tissues
479 with Ce3D multiplex volume imaging. *Nat. Protoc.* **14**, 1708–1733 (2019).
480 17. Ballesteros, I. *et al.* Co-option of Neutrophil Fates by Tissue Environments. *Cell* **183**,
481 1282-1297.e18 (2020).
482 18. Bae, G. H. *et al.* Unique characteristics of lung-resident neutrophils are maintained
483 by PGE2/PKA/Tgm2-mediated signaling. *Blood* **140**, 889–899 (2022).
484 19. De Donatis, M., Fercoq, F. & Carlin, L. M. Imaging Inflammation by Intravital
485 Microscopy. in *Imaging Inflammation* (eds. Man, F. & Cleary, S. J.) 223–241 (Springer
486 International Publishing, Cham, 2023).
487 20. Devi, S. *et al.* Multiphoton imaging reveals a new leukocyte recruitment paradigm in
488 the glomerulus. *Nat. Med.* **19**, 107–112 (2013).
489 21. Auffray, C. *et al.* Monitoring of Blood Vessels and Tissues by a Population of
490 Monocytes with Patrolling Behavior. *Science* **317**, 666–670 (2007).
491 22. Bouti, P. *et al.* β2 Integrin Signaling Cascade in Neutrophils: More Than a Single
492 Function. *Front. Immunol.* **11**, (2021).
493 23. Conrad, C. *et al.* ADAM8 signaling drives neutrophil migration and ARDS severity.
494 *JCI Insight* **7**, (2022).
495 24. Lämmermann, T. *et al.* Rapid leukocyte migration by integrin-independent flowing
496 and squeezing. *Nature* **453**, 51–55 (2008).

497 25. Petrovich, E. *et al.* Lung ICAM-1 and ICAM-2 support spontaneous intravascular
498 effector lymphocyte entrapment but are not required for neutrophil entrapment or
499 emigration inside endotoxin-inflamed lungs. *FASEB J.* **30**, 1767–1778 (2016).
500 26. Yipp, B. G. *et al.* The lung is a host defense niche for immediate neutrophil-mediated
501 vascular protection. *Sci. Immunol.* **2**, eaam8929 (2017).
502 27. Varga, G. *et al.* Active MAC-1 (CD11b/CD18) on DCs inhibits full T-cell activation.
503 *Blood* **109**, 661–669 (2006).
504 28. Headley, M. B. *et al.* Visualization of immediate immune responses to pioneer
505 metastatic cells in the lung. *Nature* **531**, 513–517 (2016).
506 29. McDonald, B. *et al.* Systemic inflammation increases cancer cell adhesion to hepatic
507 sinusoids by neutrophil mediated mechanisms. *Int. J. Cancer* **125**, 1298–1305 (2009).
508 30. Spicer, J. D. *et al.* Neutrophils Promote Liver Metastasis via Mac-1–Mediated
509 Interactions with Circulating Tumor Cells. *Cancer Res.* **72**, 3919–3927 (2012).
510 31. El Amki, M. *et al.* Neutrophils Obstructing Brain Capillaries Are a Major Cause of No-
511 Reflow in Ischemic Stroke. *Cell Rep.* **33**, 108260 (2020).
512 32. Cruz Hernández, J. C. *et al.* Neutrophil adhesion in brain capillaries reduces cortical
513 blood flow and impairs memory function in Alzheimer's disease mouse models. *Nat.*
514 *Neurosci.* **22**, 413–420 (2019).
515 33. Inwon Park *et al.* Neutrophils disturb pulmonary microcirculation in sepsis-induced
516 acute lung injury. *Eur. Respir. J.* **53**, 1800786 (2019).
517 34. Matlung, H. L. *et al.* Neutrophils Kill Antibody-Opsonized Cancer Cells by
518 Trogoptosis. *Cell Rep.* **23**, 3946-3959.e6 (2018).
519 35. Millar, R. *et al.* The MSP-RON axis stimulates cancer cell growth in models of triple
520 negative breast cancer. *Mol. Oncol.* **14**, 1868–1880 (2020).
521 36. McCowan, J. *et al.* The transcription factor EGR2 is indispensable for tissue-specific
522 imprinting of alveolar macrophages in health and tissue repair. *Sci. Immunol.* **6**, (2021).
523 37. Fercoq, F. *et al.* IL-4 receptor dependent expansion of lung CD169+ macrophages in
524 microfilaria-driven inflammation. *PLoS Negl. Trop. Dis.* **13**, (2019).

525 38. Fercoq, F. *et al.* Microfilaria-dependent thoracic pathology associated with
526 eosinophilic and fibrotic polyps in filaria-infected rodents. *Parasit. Vectors* **13**, (2020).
527 39. Li, W., Germain, R. N. & Gerner, M. Y. Multiplex, quantitative cellular analysis in
528 large tissue volumes with clearing-enhanced 3D microscopy (Ce3D). *Proc. Natl. Acad.*
529 *Sci.* **114**, E7321–E7330 (2017).
530 40. Bankhead, P. *et al.* QuPath: Open source software for digital pathology image
531 analysis. *Sci. Rep.* **7**, 16878 (2017).

532

Acknowledgments

We are grateful for support from all the services and resources at the CRUK Scotland Institute with particular thanks to the Biological Services Unit, the Beatson Advanced Imaging Resource (BAIR), the Flow Cytometry Facility and the Histology Facility. We also thank the MNHN light microscopy facility (CeMIM, Centre de Microscopie et d'IMagerie numérique, MNHN Paris) for providing access to Confocal scanning laser microscopes. We thank Jos Jonkers for the KP mammary cancer mouse model. We are grateful to Catherine Winchester for critical reading and checking of the manuscript. Illustrations were created with BioRender.com.

Data availability

Upon publication, all data will be made available by the corresponding author at reasonable request.

Competing interests

LMC has consulted for Ono Pharmaceuticals UK, JBGM has subsequently become an employee of AstraZeneca, AJM has subsequently become an employee of Antibody Analytics

Funding

FF, GSC, SBC & LMC were supported by Breast Cancer Now grant 2019DecPR1424.
CRUK Scotland Centre core - CTRQQR-2021\100006
LMC, FF, GSC, MDD, JBGM, XLRI, AM, LWGA – CRUK SI core A23983
JCN, DW - CRUK Core A28291
CN - CRUK SI core A31287
LB – Wellcome Trust Biomedical Vacation Scholarship
EWR - CRUK core A1920
KB - CRUK Core A29799 CRUK SI CRUK core - A31287

Author contributions

Conceptualization – FF, GSC, SBC, LMC
Formal analysis – FF, GSC
Funding acquisition- JCN, EWR, KB, SBC, LMC
Investigation – FF, GSC, MDD, RW, JBGM, AF, AM, XLR, DW, LWGA, CN, AK, LB, SA-K
Methodology – FF, KB, SC
Project administration – LMC
Resources – RW, AK, SBC
Supervision – JCN, EWR, KB, SBC, LMC
Validation – FF, GSC, DW

Visualization – FF, GSC

Writing – original draft – FF, GSC, LMC.

571 **Figures**

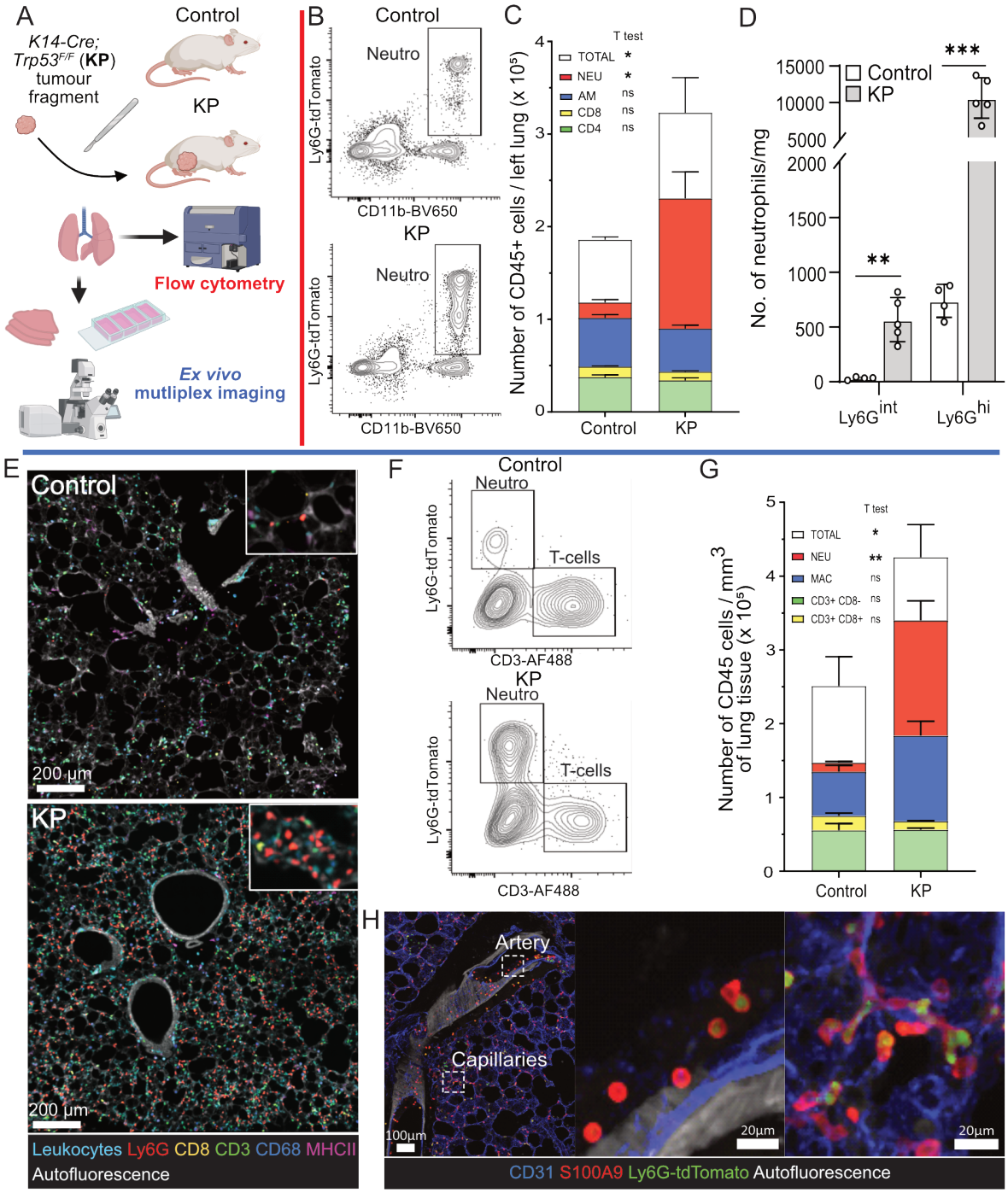

572

573 **Figure 1: The pre-metastatic lung is congested with neutrophils.**

574 (A) Schematic of tumour transplant model and experimental setup.

575 (B-C) Flow cytometry analysis of lungs (using lung immunophenotyping panel) from age-matched non-
576 transplanted control and orthotopic KP 10-15 mm tumour-bearing Catchup$^{IVM\text{-}red}$ Ly6G reporter mice.
577 (B) Representative gated plots of CD11b^{+} Ly6G$^{tdtomato+}$ neutrophils, see **Figure S2A** for full gating
578 strategy. (C) Quantification of the different CD45^{+} cell populations. NEU: neutrophils; AM: alveolar
579 Macrophages; CD8: CD8+ T-lymphocytes, CD4: CD4+ T-Lymphocytes. Results are expressed as

580 mean ± SEM of n = 3 control and 6 tumour-bearing Catchup$^{IVM-red}$ mice. T-tests were performed for
581 each cell type, *p≤0.05.
582 (D) Flow cytometry analysis of neutrophil maturity (using neutrophil phenotyping panel 1) through Ly6G
583 expression level in the lungs from orthotopic KP 10-15 mm tumour-bearing mice. Results are expressed
584 as mean ± SD of n = 4 control and 5 10-15 mm tumour-bearing Catchup$^{IVM-red}$ mice. See **Figure S2B**
585 for gating strategy. T-tests were performed for Ly6G^{int} control vs KP and Ly6G^{hi} control vs KP, **p≤0.01
586 and *** p≤0.001.
587 (E-G) Chemically cleared precision-cut lung slices (PCLS) were investigated by spectral multiplexed
588 immunofluorescence confocal microscopy and images were analysed as in **Figure S2C**. (E) Maximum
589 intensity projections of spectrally unmixed PCLS images stained with CD3-AF488, CD8-Cy3, CD68-
590 AF594, MHCII-BV421 and a mix of CD45+CD19+CD11c-AF647 in addition to the tdTomato reporter for
591 Ly6G. Autofluorescence was also unmixed and provided tissue architecture information. (E) Leukocytes
592 were segmented, and cell fluorescence intensity was imported in a flow-cytometry analysis software.
593 Figure shows representative plots. (G) Quantification of the different cell populations by histocytometry
594 of fluorescence images. Results are expressed as mean ± SEM of n = 3 control and 6 tumour-bearing
595 mice Catchup$^{IVM-red}$ mice. T-tests were performed for each cell type, *p≤0.05, **p≤0.01.
596 (H) Fixed precision cut lung slices (PCLS) were imaged for neutrophils (S100A9 and Ly6G^{tdTomato}) along
597 with CD31 (blue) staining of vascular endothelium. Dashed squares indicate zoomed on an artery area
598 showing round neutrophils or constricted neutrophils in capillaries.
599 Flow cytometry (B-C) and (D) and imaging results (E-H) were obtained from three independent
600 experiments.
601

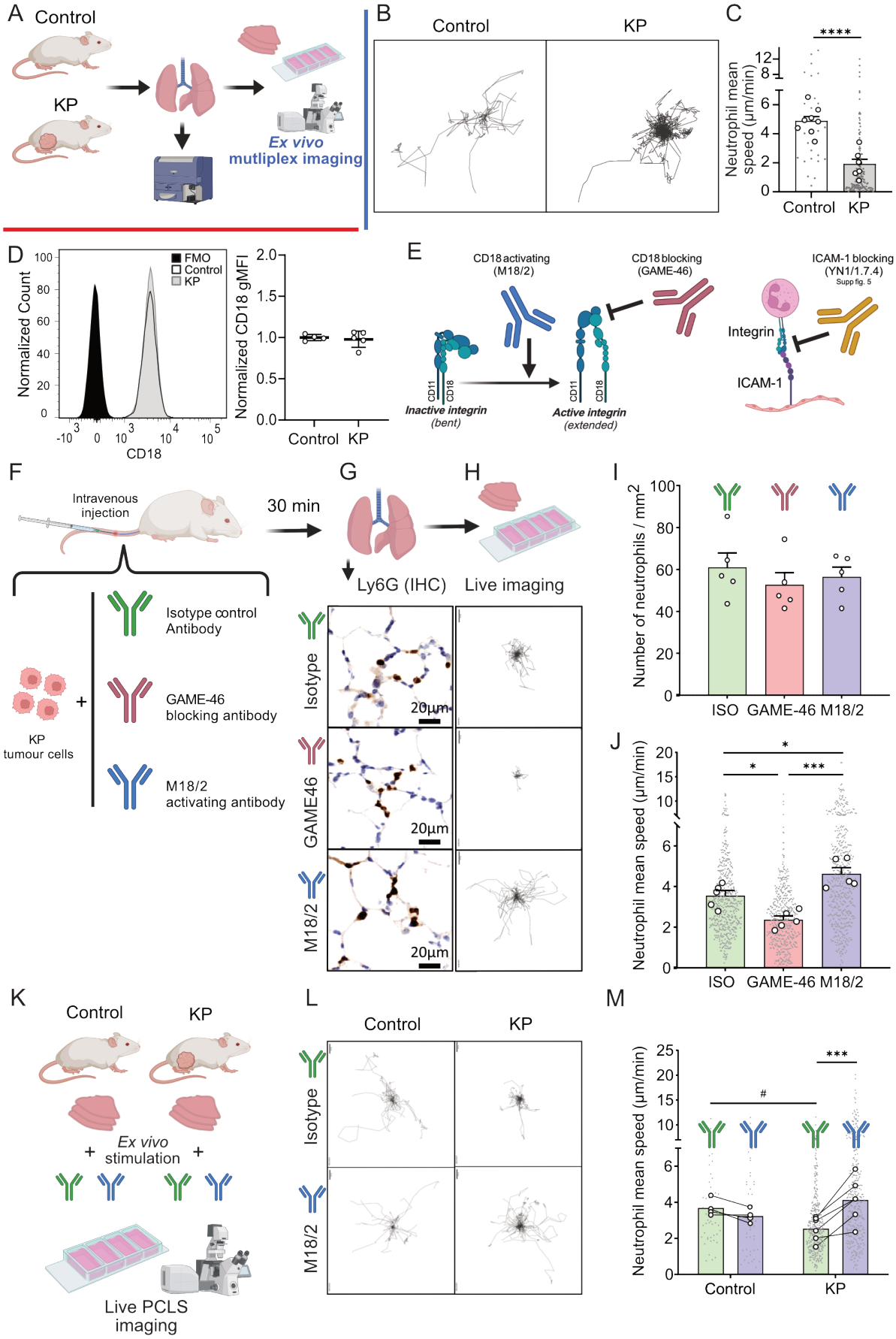
A
Control
KP
Ex vivo
mutliplex imaging
B
Control
KP
C
****
Neutrophil mean speed (µm/min)
Control
KP
D
FMO
Control
KP
Normalized Count
CD18
Normalized CD18 gMFI
Control
KP
E
CD18 activating (M18/2)
CD18 blocking (GAME-46)
ICAM-1 blocking (YN1/1.7.4)
Supp fig. 5
Integrin
ICAM-1
CD11
CD18
Inactive integrin (bent)
Active integrin (extended)
F
Intravenous injection
30 min
KP tumour cells
Isotype control Antibody
GAME-46 blocking antibody
M18/2 activating antibody
G
Ly6G (IHC)
H
Live imaging
Isotype
GAME46
M18/2
20µm
I
Number of neutrophils / mm2
ISO
GAME-46
M18/2
J
Neutrophil mean speed (µm/min)
ISO
GAME-46
M18/2
K
Control
KP
Ex vivo stimulation
Live PCLS imaging
L
Control
KP
Isotype
M18/2
M
Neutrophil mean speed (µm/min)
***
#
Control
KP

603 **Figure 2: Neutrophils in the pre-metastatic are slow-moving due to integrin inactivation.**

604 (A) Schematic of the experiment design. Lungs from age-matched non-transplanted control and 10-15
605 mm orthotopic KP tumour-bearing FVB/N mice were harvested for live precision-cut lung slices (PCLS)
606 imaging or flow cytometry.
607 (B-C) Neutrophil tracking in live multiplexed confocal microscopy timelapse images of *ex vivo* PCLS
608 from control and KP tumour-bearing mice (see video S1). (B) Representative neutrophil tracking centred
609 plots (spider plot). (C) Quantification of neutrophil mean speed. Grey dots represent the speed of each
610 individual neutrophil (24-148 tracks per group were analysed) while white dots represent the mean
611 speed in each mouse. The mean value per animal were used to perform an unpaired parametric t
612 test.****$p \leq 0.0001$. Results are expressed as mean +/- SEM of n = 8 control and 6 tumour-bearing FVB/N
613 mice.
614 (D) Flow cytometry analysis of CD18 expression on lung neutrophils (using neutrophil phenotyping
615 panel 1). Left: representative histogram. Right: quantification of CD18 geometric mean fluorescence
616 intensity (gMFI). Results are expressed as mean +/- SD of n = 4 control and 5 tumour-bearing
617 Catchup$^{IVM\text{-}red}$ mice. Fluorescence minus one (FMO) for CD18 also shown. See **Figure S2B** for gating
618 strategy. A nonparametric Mann-Whitney test was performed, ns>0.05.
619 (E) Schematic of integrin conformational changes controlling integrin activation and integrin binding to
620 ICAM-1. The M18/2 antibody stabilizes the active conformation, whereas the GAME-46 antibody blocks
621 the CD18 active domain. YN1/1.7.4 antibody blocks ICAM-1 (see **Figure S6**).
622 (F-J) Modulation of neutrophil motility in an intravenous (IV) transplant model of KP cells, using CD18
623 activating and blocking antibodies. (F) Schematic of the experiment design. Mice were IV injected with
624 KP cells and either isotype control antibody (green), GAME-46 (pink), or M18/2 (blue). 30 minutes later
625 lungs were taken for live *ex vivo* confocal microscopy of PCLS (see **video S2**) and
626 Immunohistochemistry. (G) Representative IHC images from the three treatment groups. (H)
627 Representative neutrophil tracking plots from the three treatment groups. (I) Quantification of the
628 number of neutrophils/mm^2 in lung IHC images. Results are expressed as mean +/- SEM of 5 mice per
629 group. A one-way ANOVA was performed. (J) Quantification of neutrophil speed in live *ex vivo*
630 microscopy. Grey dots represent the speed of individual neutrophil (a total of 482-913 tracks per group
631 were analysed; display was cropped at 512 tracks) while white dots represent the mean neutrophil
632 speed per mouse. The mean value per mouse were used to perform an ANOVA. (G-J) Results are
633 expressed as mean +/- SEM of n = 5 mice per group, pool of 5 independent experiments with 1 mouse
634 per group. *$p \leq 0.05$, ***$p \leq 0.001$.
635 (K-M) *Ex vivo* stimulation of live PCLS from control and KP tumour-bearing mice. (K) Schematic of the
636 experiment design. Live lungs from age-matched controls and 10-15 mm KP-tumour bearing mice were
637 inflated with low-melting point agarose, live PCLS were sliced using a vibratome and stimulated with
638 either isotype control antibody or M18/2 in a chamber slide. (L) Representative neutrophil tracking plots.
639 (M) Quantification of neutrophil mean speed. Grey dots represent the speed of individual neutrophils (a
640 total of 44-371 tracks per group were analysed) while white dots represent the mean neutrophil speed
641 per mouse. Results are expressed as mean +/- SEM of n =4 control mice and 6 KP-tumour bearing
642 Catchup$^{IVM\text{-}red}$ mice. A Two-way Repeated Measure ANOVA followed with Sídák's multiple

643 comparisons tests was performed. *** $p \leq 0.001$ for differences between isotype and M18/2 antibodies,
644 $^{\#}p \leq 0.05$ for differences between control and KP tumour bearing mice.
645

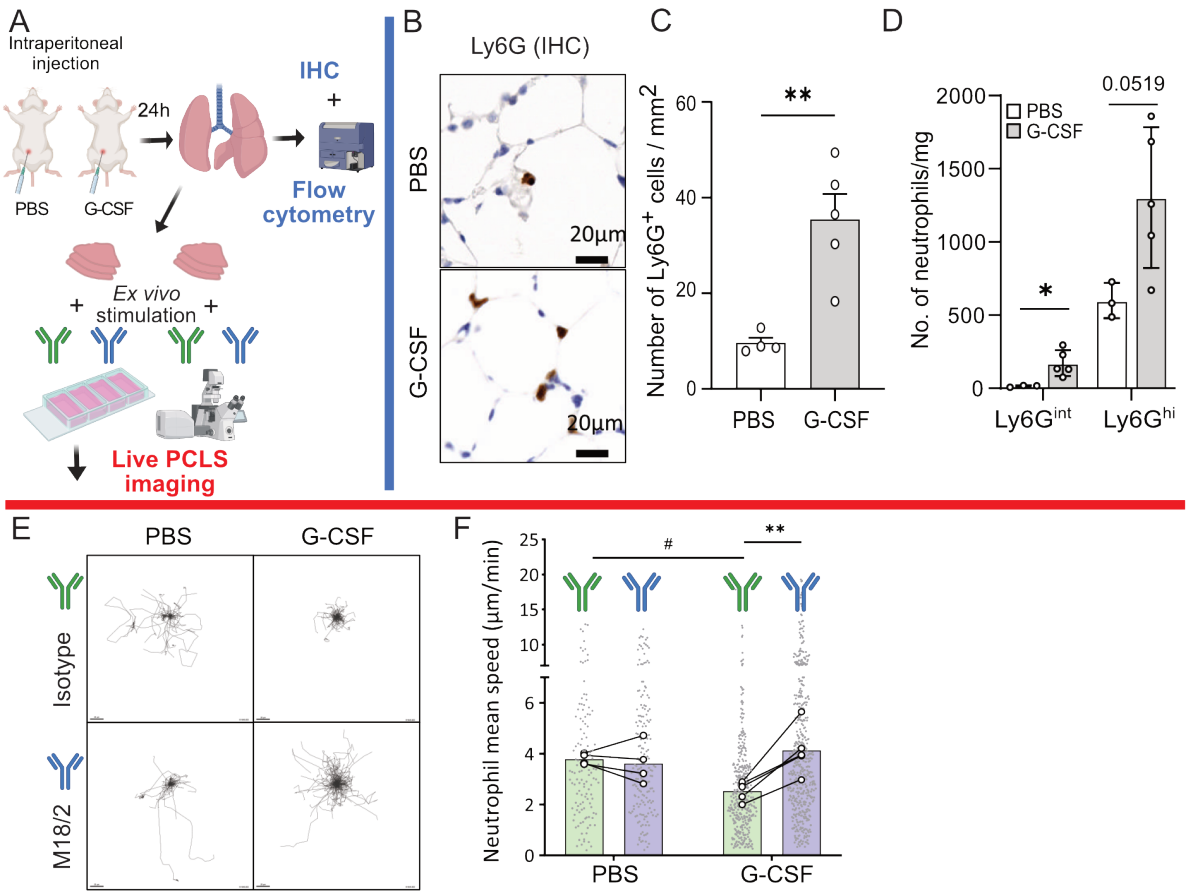

Figure 3: G-CSF induces mobility inhibition by impairing CD18 activation.

(A) Schematic of experiment design. Mice were IP injected with either PBS or 5 µg G-CSF. 24 hours later lungs were taken for IHC, flow cytometry and/or live *ex vivo* multiplexed confocal microscopy of PCLS stimulated with either isotype control or M18/2.

(B) Representative Ly6G IHC images from PBS and G-CSF treated FVB/N mice.

(C) Quantification of number of $Ly6G^+$ cells (neutrophils)/mm^2 of lung tissue in IHC images. Results are expressed as mean +/- SEM of n = 4 PBS control and 5 G-CSF treated mice. An unpaired parametric t test was performed. **p≤0.01.

(D) Flow cytometry analysis (using neutrophil phenotyping panel 1) of lung neutrophil maturity based on Ly6G expression level. Results are expressed as mean ± SD of n = 3 control and 5 G-CSF treated $Catchup^{IVM\text{-}red}$ mice. See **Figure S2B** for gating strategy. T-tests were performed for $Ly6G^{int}$ control vs G-CSF and $Ly6G^{hi}$ control vs G-CSF, *p≤0.05.

(E) Representative neutrophil tracking plots of live PCLS from PBS and G-CSF treated FVB/N mice, stimulated *ex vivo* with either isotype antibodies or M18/2.

(F) Quantification of mean neutrophil speed from live multiplexed confocal microscopy. Grey dots represent the speed of individual neutrophils (a total of 128-482 tracks per group were analysed) while white dots represent the mean speed per mouse. A Two-way Repeated Measure ANOVA followed with Sídák's multiple comparisons test was performed on the mean values. Results are expressed as mean +/- SEM of n = 4 PBS control and 5 G-CSF treated FVB/N mice (same mice as in B-C). ** p≤0.01 for

666 differences between isotype and M18/2 antibodies, #p≤0.05 for differences between control and G-CSF
667 treated mice.

668

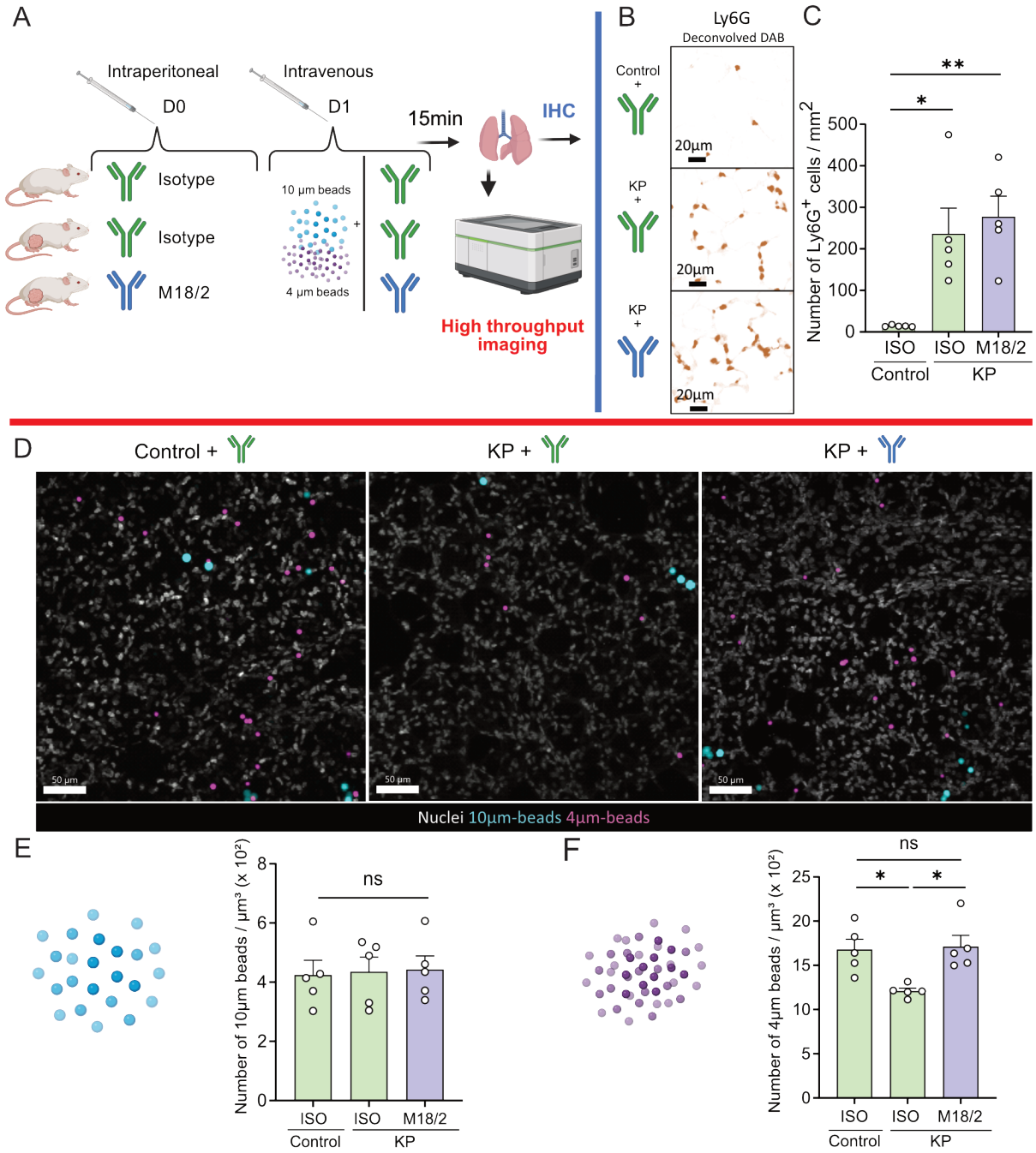

669

670 **Figure 4. Slowed neutrophils in the pre-metastatic lung restricts blood flow.**

671 (A) Schematic of experiment design. 4- and 10-µm fluorescent beads were intravenously injected to
672 control and KP tumour-bearing FVB/N mice along with with either M18/2 or isotype control antibodies.
673 Lungs were there harvested for (B-C) Ly6G IHC quantification and (D-F) high throughput confocal
674 fluorescence imaging of fixed PCLS.

675 (B) Representative IHC images from the three different experiment groups. (C) Quantification of the
676 number of $Ly6G^+$ cells per mm^2 of lung tissue. Results are expressed as mean +/- SEM of n = 5 mice
677 per group. A one-way ANOVA with Šídák's multiple comparison test was carried out (*p≤0.05, and
678 **p≤0.01).
679 (D-F) High throughput confocal fluorescence imaging of fixed PCLS to quantify number of beads in the
680 slices. (D) Representative individual field of views for the three experiment groups where DNA was
681 labelled with DRAQ5. (E) Quantification of the number of 10µm beads per $µm^3$. (F) Quantification of the
682 number of 4µm beads per $µm^3$. Results are expressed as mean +/- SEM of n = 5 mice per group (same
683 mice as in B-C). A one-way ANOVA with Šídák's multiple comparison tests was carried out (*p≤0.05).
684

685 **Supplementary figures and legends**

686 **Video 1: Neutrophil behaviour and free radical production in live PCLS.**

687 Lungs from 10-15 mm KP tumour bearing mice were harvested for live *ex vivo* multiplexed confocal
688 microscopy of PCLS to analyse their behaviour and free radical production (Reactive Oxygen Species
689 – ROS and Reactive Nitrogen Species – RNS). Slices were stained for DNA (Hoechst, blue),
690 vasculature (CD31, grey) and neutrophils (Ly6G, red) as well as probes for ROS (orange) and RNS
691 (yellow). 5 minutes timelapse series were acquired and neutrophils were tracked using Imaris software.

692 **Video 2: CD18 modulates lung neutrophil motility in an intravenous transplant model of KP cells.**

693 Catchup$^{IVM\text{-}red}$ mice were IV injected with KP cells stained with cellTrace dyes (yellow) and either
694 isotype control antibody, CD18 blocking antibody (GAME-46) or CD18 activating antibody (M18/2). 30
695 minutes later lungs were taken for live *ex vivo* confocal microscopy of PCLS. Slices were stained for
696 DNA (Hoechst, blue), vasculature (CD31, grey), neutrophils (Ly6G, purple) and CD45 (cyan). 40
697 minutes timelapse series were acquired, and neutrophils were tracked using Imaris software.

698 **Video 3: ICAM-1 modulates lung neutrophil motility in an intravenous transplant model of KP**
699 **cells.**

700 Catchup$^{IVM\text{-}red}$ mice were IV injected with KP cells stained with cellTrace dyes (yellow) and either
701 isotype control antibody or ICAM-1 blocking antibody. 30 minutes later lungs were taken for live *ex vivo*
702 confocal microscopy of PCLS. Slices were stained for DNA (Hoechst, blue), vasculature (CD31, grey),
703 neutrophils (Ly6G, purple) and CD45 (cyan). 8 minutes timelapse series were acquired, and neutrophils
704 were tracked using Imaris software.

705 **Video 4: CD18 modulates lung neutrophil motility in tumour bearing mice.**

706 Lungs from 10-15 mm KP tumour bearing Catchup$^{IVM\text{-}red}$ mice were harvested for live *ex vivo*
707 multiplexed confocal microscopy of PCLS and stimulated *ex vivo* with either isotype control antibody or
708 CD18 activating antibody (M18/2). Slices were stained for DNA (Hoechst, blue), vasculature (CD31,
709 grey), neutrophils (Ly6G-td Tomato, purple), T-cells (CD8, green), alveolar macrophages (CD11c,
710 orange) and leukocytes (CD45, cyan). 30 minutes timelapse series were acquired, and neutrophils were
711 tracked using Imaris software.

712 **Video 5: G-CSF treatment modulates lung neutrophil motility in a CD18 dependent manner.**

713 Lungs from G-CSF treated mice were harvested for live *ex vivo* multiplexed confocal microscopy of
714 PCLS and stimulated *ex vivo* with either isotype control antibody or CD18 activating antibody (M18/2).
715 Slices were stained for DNA (Hoechst, blue), vasculature (CD31, grey) and neutrophils (Ly6G, purple).
716 15 minutes timelapse series were acquired, and neutrophils were tracked using Imaris software.

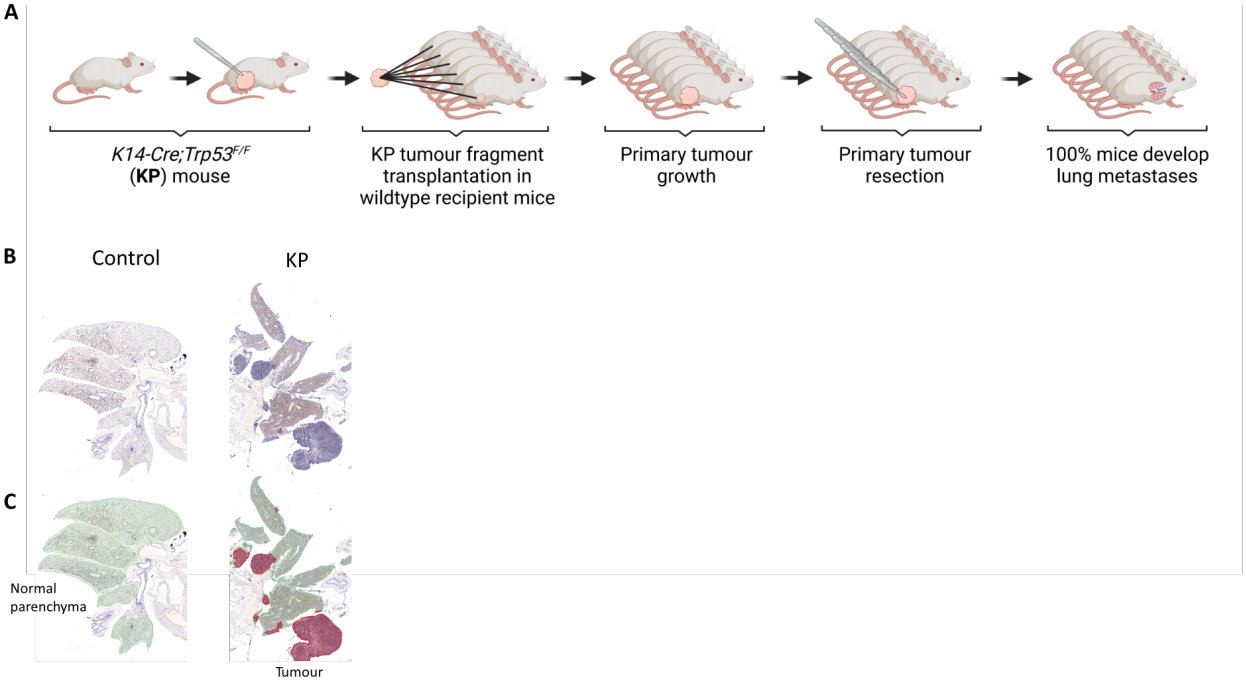

Figure S1: Spontaneous metastasis model.

A) Mammary tumour fragments from KP mice were orthotopically transplanted into WT recipient mice, allowed to grow, then surgically resected when tumour reached 10mm in any direction. Metastases develop in 100% of recipient mice.

B) Representative hematoxylin & eosin staining from non-transplanted control and metastatic lungs.

C) Annotation showing normal parenchyma (green) and tumour tissue (red) from a pixel classification in QuPath[40].

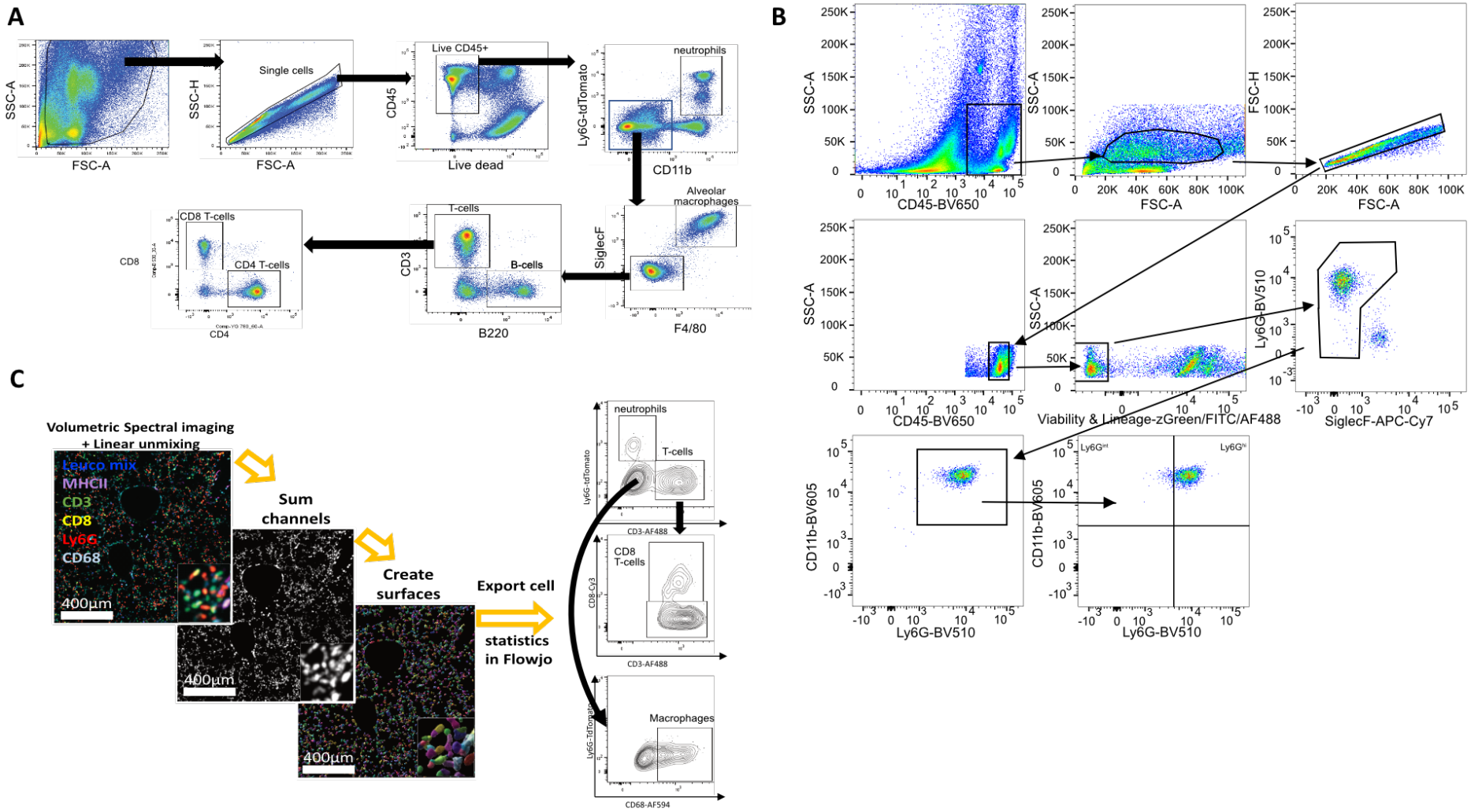
A
SSC-A
FSC-A
SSC-H
Single cells
CD45
Live CD45+
Live dead
Ly6G-tdTomato
neutrophils
CD11b
SiglecF
Alveolar macrophages
F4/80
CD3
T-cells
B-cells
B220
CD8
CD8 T-cells
CD4 T-cells
CD4
B
CD45-BV650
FSC-A
FSC-H
Viability & Lineage-zGreen/FITC/AF488
SiglecF-APC-Cy7
Ly6G-BV510
CD11b-BV605
C
Volumetric Spectral imaging
+ Linear unmixing
Leuco mix
MHCII
CD3
CD8
Ly6G
CD68
400µm
Sum
channels
Create
surfaces
Export cell
statistics
in Flowjo
neutrophils
T-cells
CD8
T-cells
Macrophages
CD3-AF488
CD68-AF594

728 **Figure S2: Gating strategies for flow cytometry and Histocytometry.**
729 A) Gating strategy for flow cytometry analysis of dissociated lung to phenotype CD45+ immune cell
730 populations: Neutrophils (CD11b+ Ly6G+), Alveolar macrophages (CD11b- SiglecF+), B- cells (B220+),
731 CD8 T-cells (CD3+ CD8+) and CD4 T-cells (CD3+ CD4+). Relevant to Figure 1.
732 B) Gating strategy for flow cytometry analysis of $Ly6G^{int}$ and $Ly6G^{hi}$ neutrophil numbers and CD18
733 neutrophil surface expression in Figures 1, 2 and 3.
734 C) Histocytometry strategy for analysing lung tissue images in Figure 1E-G. Fixed precision cut lung
735 slices (PCLS) were stained with fluorescently labelled antibodies and imaged with a spectral confocal
736 microscope. After linear unmixing of the different fluorophores, the channels corresponding to the
737 different immune markers were summed to allow the segmentation of all immune cells in Imaris
738 software. Cell statistics were then imported into FlowJo for analysis. Data shown here is from Figure
739 1E for illustration purposes.
740
741
742
743

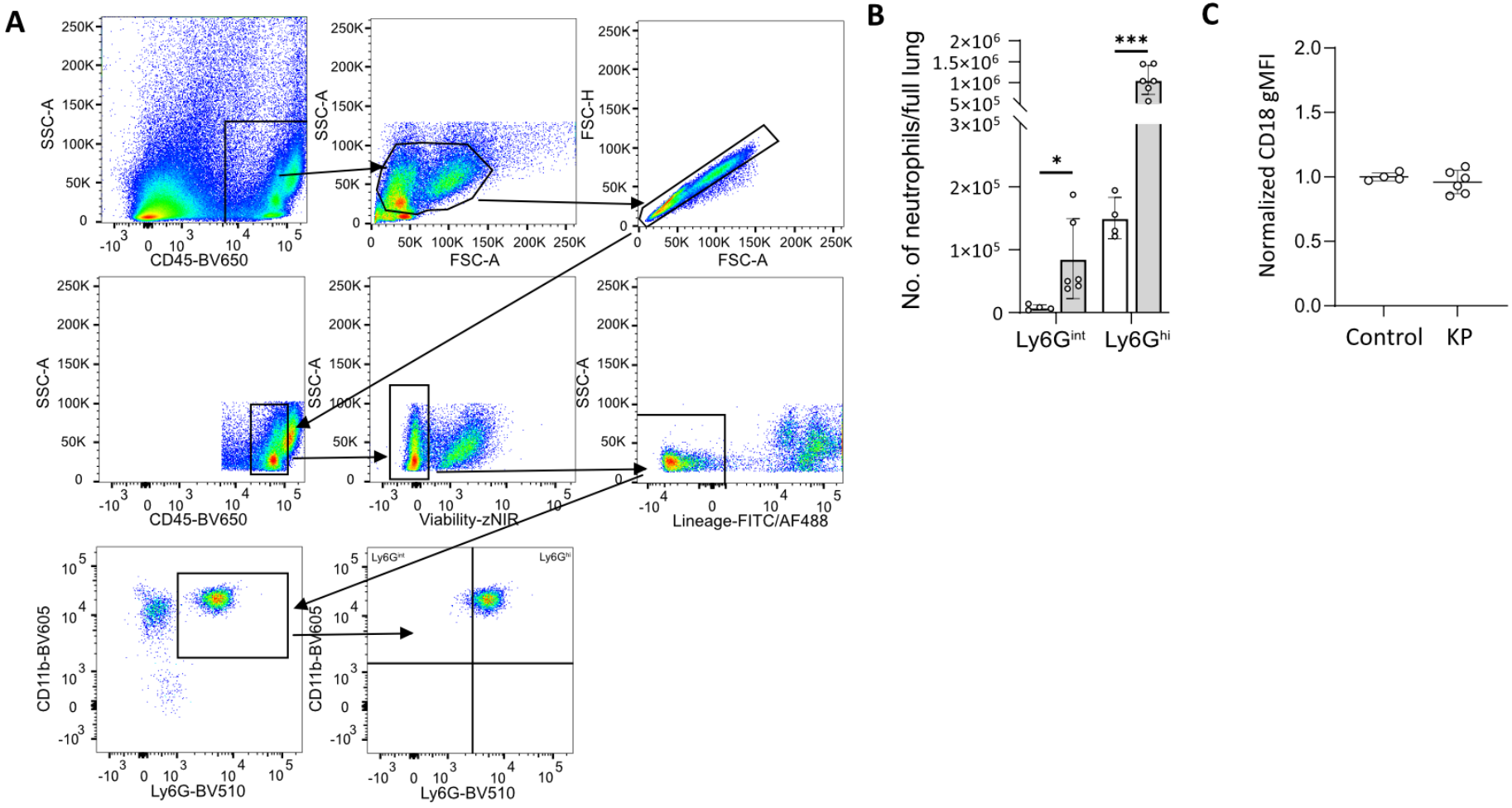
A
SSC-A
CD45-BV650
FSC-A
FSC-H
Viability-zNIR
Lineage-FITC/AF488
CD11b-BV605
Ly6G-BV510
Ly6G^int
Ly6G^hi
B
No. of neutrophils/full lung
Ly6G^int
Ly6G^hi
C
Normalized CD18 gMFI
Control
KP

745 **Figure S3: Gating strategies for flow cytometry of WT FVB/N mice.**
746 A) Gating strategy for flow cytometry analysis of $Ly6G^{int}$ and $Ly6G^{hi}$ neutrophil numbers and CD18
747 neutrophil surface expression.
748 B) Flow cytometry analysis of neutrophil maturity (using neutrophil phenotyping panel 2) through Ly6G
749 expression level in the lungs from orthotopic KP 10-15 mm tumour-bearing mice. Results are expressed
750 as mean ± SD of n = 4 control and 6 10-15 mm tumour-bearing WT FVB/N mice. See **Figure S3A** for
751 gating strategy. T-tests were performed for $Ly6G^{int}$ control vs KP and $Ly6G^{hi}$ control vs KP, *$p \leq 0.05$ and
752 *** $p \leq 0.001$.
753 C) Flow cytometry quantification of CD18 geometric mean fluorescence intensity (gMFI) on lung
754 neutrophils (using neutrophil phenotyping panel 2). Results are expressed as mean +/- SD of n = 4
755 control and 6 10-15 mm tumour-bearing WT FVB/N mice. See **Figure S3A** for gating strategy. A
756 nonparametric Mann-Whitney test was performed, ns>0.05.
757
758
759

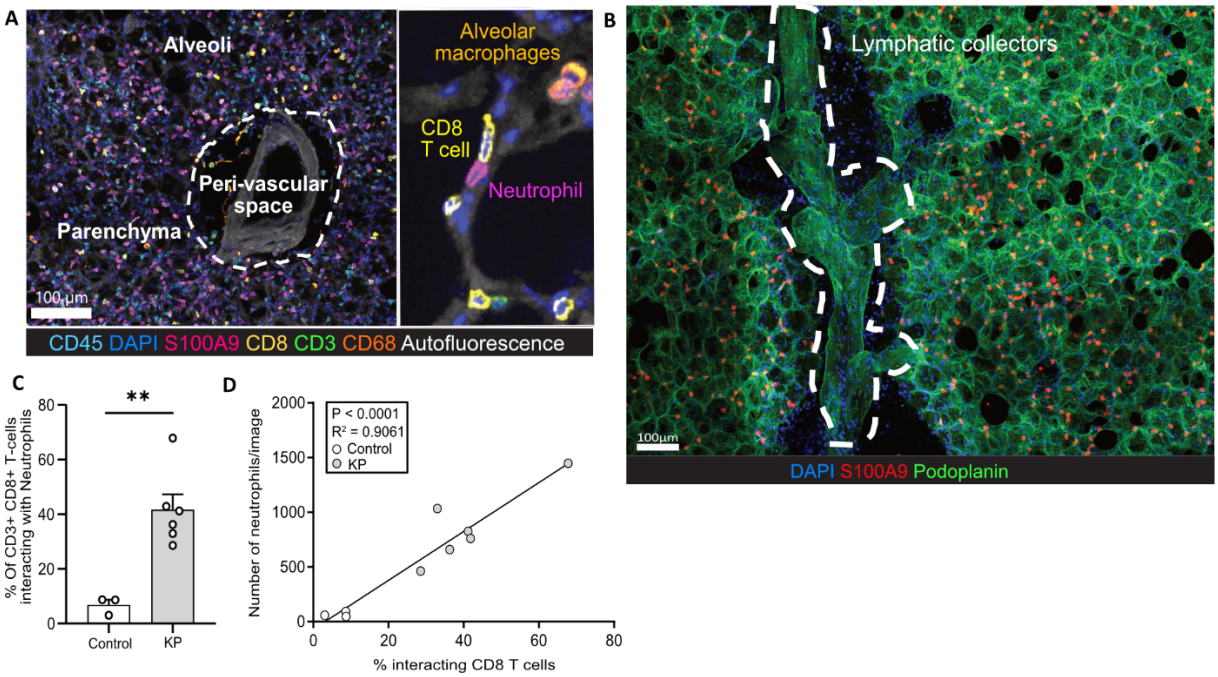

Figure S4: Localisation of lung neutrophils and CD8 T-cells interactions.

A) Maximum intensity projection of a spectrally unmixed multiplexed confocal microscopy image of a PCLS from a KP tumour bearing FVB/N mouse stained with CD45-Dylight685, DAPI, S100A9-AF700, CD8-Cy3, CD3-AF488 and CD68-AF594. Autofluorescence was also unmixed and provided tissue architecture information. The close-up view of the lung parenchyma shows neutrophil-CD8$^+$ T cell interaction in lung capillaries.

B) Podoplanin (green) staining for lymphatic collectors (it also stains alveolar cells in the lung) in a PCLS from a KP tumour bearing FVB/N mouse. S100A9 (red) was used to stain neutrophils and DAPI (blue) was used to stain DNA.

C) Quantification of neutrophil-T-cell interactions in PCLS from control and KP-tumour Catchup$^{IVM\text{-}red}$ bearing mice. Results are expressed as mean ± SEM of n = 3 control and 6 tumour-bearing mice (related to images in figure 1E-G), T-test **p<0.01.

D) The correlation between CD8$^+$ T cell:neutrophil interaction and neutrophil numbers was analysed using the Spearman's rank correlation test (r = 0.8333 p=0.0083); then a linear regression was performed to describe relationship between variables, showing that 90% (R^2= 0,9061, p<0.0001) of the interactions can be significantly explained by the number of neutrophils in the lung.

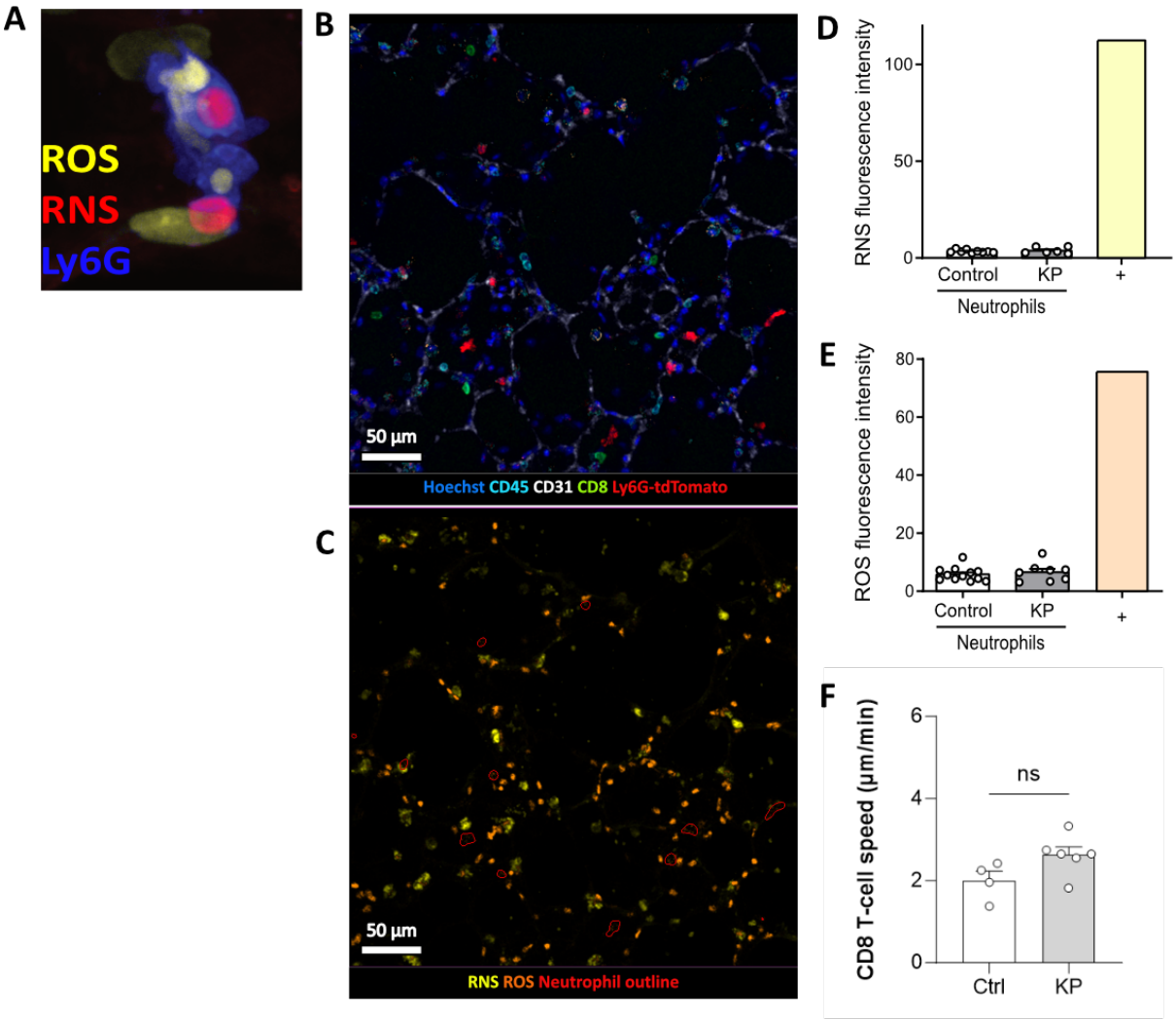

Figure S5: ROS/RNS production in live PCLS and CD8 T-cell speed.

Lungs from control and KP tumour bearing mice were harvested for live *ex vivo* multiplexed confocal microscopy of PCLS to analyse their behaviour and free radical production (Reactive Oxygen Species – ROS and Reactive Nitrogen Species – RNS).

(A) Positive control from a Phorbol 12-myristate 13- acetate (PMA) treated PCLS showing a neutrophil (Ly6G, blue) with cytoplasmic ROS (yellow) and nuclear RNS (red).

(B-C) Slices were stained for DNA (Hoechst, blue), vasculature (CD31, grey), CD8 T-cells (CD8, green), leukocytes (CD45, cyan) and neutrophils (Ly6G, red) as well as probes for ROS (orange) and RNS (yellow).

(D) Quantification of RNS mean fluorescence intensity in neutrophils. The + bar represents the mean intensity from a surrounding RNS positive cell.

(E) Quantification of ROS mean fluorescence intensity in neutrophils. The + bar represents the mean intensity from a surrounding ROS positive cell.

(D-E) Results are expressed as mean +/- SEM of n = 8-12 mice per group.

792 (F) CD8 T-cells mean speed in Control and KP orthotopic tumour-bearing mouse lung slices. Results
793 are expressed as mean +/- SEM of n = 4 control mice and 6 KP-bearing mice. A parametric t-test was
794 performed, ns $p>0.05$.

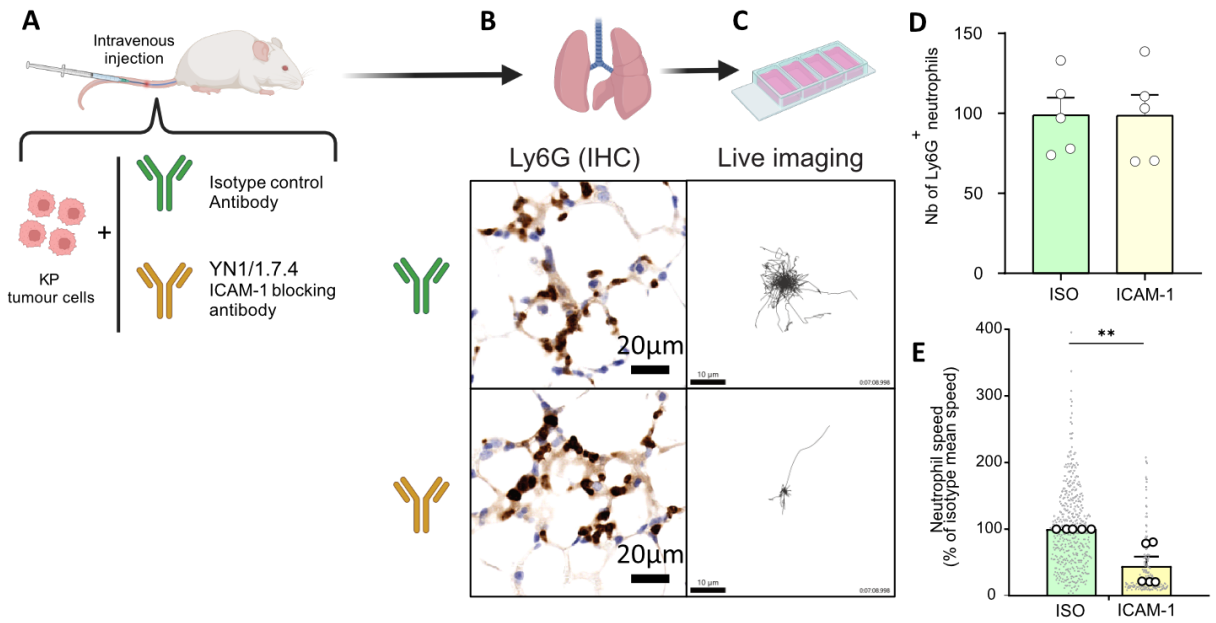

Figure S6: Modulation of neutrophil motility in an intravenous (IV) transplant model of KP cells, using ICAM-1 blocking antibodies.

(A) Schematic of the experiment design. Mice were IV injected with KP cells and either isotype control antibody (green) or ICAM-1 blocking antibodies (yellow). 30 minutes later lungs were taken for live *ex vivo* confocal microscopy of PCLS (see video S3) and Immunohistochemistry.

(B) Representative IHC images from the two treatment groups.

(C) Representative neutrophil tracking plots from the two treatment groups.

(D) Quantification of the number of neutrophils/mm^2 in lung IHC images. Results are expressed as mean +/- SEM of 5 mice per group. A t-test was performed.

(E) Quantification of neutrophil speed as a % of the isotype control mean speed from live *ex vivo* microscopy. Grey dots represent the speed of each individual neutrophil (a total of 213-459 tracks per group were analysed) while white dots represent the mean neutrophil speed per mouse. Statistical analysis (nonparametric Mann-Whitney test) was performed on the mean value per animal. Results are expressed as mean +/- SEM of n = 5 mice per group. **$p < 0.01$.

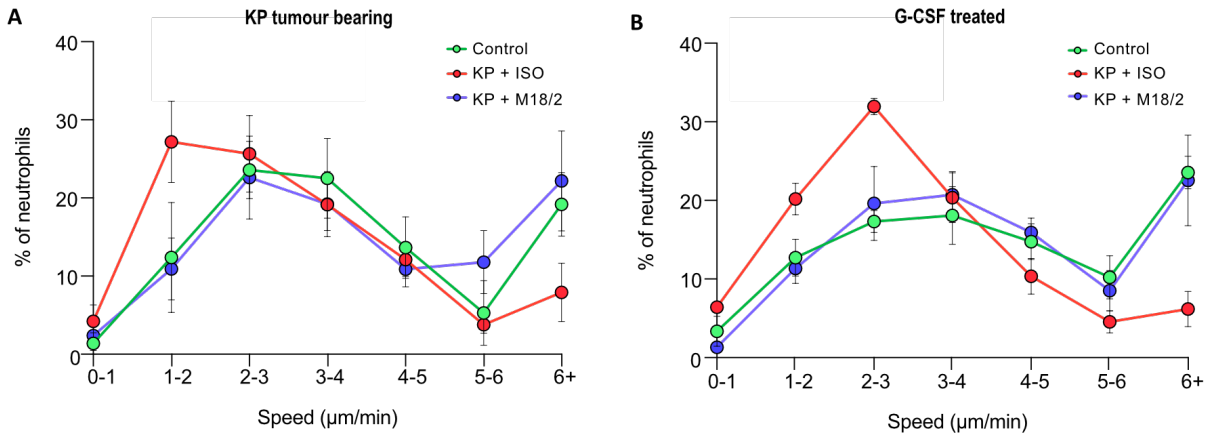

Figure S7: Neutrophil speed distribution in the lungs of mice with KP tumour and mice treated with G-CSF.

Neutrophils were tracked in live multiplexed confocal microscopy timelapse images of *ex vivo* PCLS after *ex vivo* stimulation with either isotype control antibody or M18/2.

(A) Speed distribution of neutrophils from control and KP tumour-bearing mice from Figure 2M. Results are expressed as mean +/- SEM of n = 4 control mice and 6 KP-tumour bearing mice

(B) Speed distribution of neutrophils from PBS and G-CSF treated mice from Figure 3E. Results are expressed as mean +/- SEM of n = 4 PBS control and 5 G-CSF treated mice.